Generalized Analysis for a Class of Linear Interferometric Networks—Part II: Simulations

Otto Schwelb, *Senior Life Member, IEEE*

***Abstract*— In Part I of this paper, the author presented a method to simplify the analysis and design of interferometric microwave and optoelectronic networks such as filters, sensors, ring resonators, etc., comprised of 2 × 2 couplers, waveguides, reflectors, and mismatched interfaces. The simplification was achieved by introducing a generalized single-mode lumped-element 2 × 2 coupler with arbitrary coupling paths. In Part II, the author numerically examines a number of interferometric devices utilizing the analysis described in Part I. These devices include feedback-assisted couplers, multiple-ring resonators, unit transmittance circuits, add/drop filters, grating-assisted Mach–Zehnder (M–Z) interferometers, etc. Results are presented on the characteristics of the output and circulating wave in the resonant rings as a function of frequency, coupling coefficient, loss, and other component parameters. Results on group-delay characteristics are also given.**

***Index Terms*—Filter circuits, interferometric networks, sensors.**

I. Introduction

IN PART I of this paper [1], a method was presented to analyze and evaluate a wide variety of interferometric circuits based on 2 × 2 couplers. Central to this method was the introduction of a new generalized lumped-element 2 × 2 coupler. The topological flexibility offered by this generalized coupler made it possible to treat any interferometric circuit based on 2 × 2 couplers as a cascaded set of four-ports and, consequently, to apply cascade circuit analysis to a wide variety of network topologies. Part I of this paper analyzed cascaded circuits with internal (reflective elements terminating some or all external ports) and combined internal and external (transmission circuit(s) connecting external ports) feedback, including resonant configurations. It provided unified expressions for the scattering matrix of the feedback-assisted device, for the circulating amplitude in the feedback line, and for the characterization of resonant circuits. Finally, Part I also listed the scattering transfer matrices ($\boldsymbol{A}$) of the six types of generalized lumped-element 2 × 2 couplers and the symmetry operations that relate the scattering matrices ($\boldsymbol{S}$) of these couplers to each other.

In Part II, we describe, through numerical experiments, the performance of selected devices, demonstrating the salient features of the analysis and its ease of use. In Section II, cascaded circuits without feedback are examined. Here, we compare the performance of circuits built with lumped-element and distributed parameter couplers, connected to each other through transmission lines and/or gratings (or Fabry–Perot (F–P) resonators). Section III deals with feedback-assisted circuits, including channel dropping and combining filters (add/drop filters). Transmitted intensity, circulating current, time delay, and finesse will be characterized. Special attention is paid to so-called unit-transmittance networks [2]. In Section IV, we focus on resonator circuits and on the effect of loss on resonance characteristics. Section V summarizes the advantages of the method of calculation and the results obtained.

Manuscript received March 2, 1998. This work was supported by the Natural Sciences and Engineering Research Council of Canada and by the Fonds pour la Formation de Chercheurs et l'Aide à la Recherche.

The author is with the Department of Electrical and Computer Engineering, Concordia University, Montréal, P.Q., Canada H3G 1M8.

Publisher Item Identifier S 0018-9480(98)07247-0.

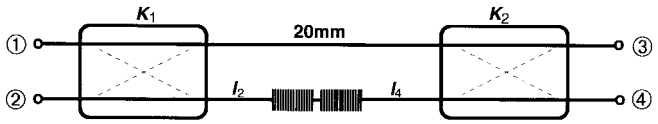

Fig. 1. M–Z interferometer with an F–P resonator built into one of the transmissions lines connecting the couplers.

II. Cascaded Circuits

The four-port network obtained by connecting the basic building blocks, namely couplers, transmission lines (waveguides, optical fibers, etc.), gratings, F–P resonators, and interface (splice) discontinuities, is called the cascaded network. Fig. 1 shows an example of such a network consisting of two lumped-element or distributed parameter forward (Type 1) couplers connected by a uniform waveguide and another guide with a built-in F–P resonator. The figure also indicates the port designation used in this paper. The network illustrated in Fig. 1 is a modified Mach–Zehnder (M–Z) interferometer, adapted to sense small changes in the phase shift in one of the arms (pigtails) of the resonator. The performance of this sensor, using fused couplers, was simulated in the infrared, near 10 μm. The power-coupling coefficients of the lossless couplers were $K_1 = K_2 = 0.5$, the length of the uniform waveguide was 20 mm, and the pigtails connecting the resonator to the couplers were $l_2 = l_4 = 10$ mm long. Each half of the resonator is made up of 40 unit cells separated by a 3.38-μm-long cavity. Each unit cell consists of two 1.62-μm-long sections, their refractive indexes being 1.5 and 1.6, respectively. The effective refractive index of the uniform line sections, including that of the cavity, was chosen to be $n_e = 1.5$.

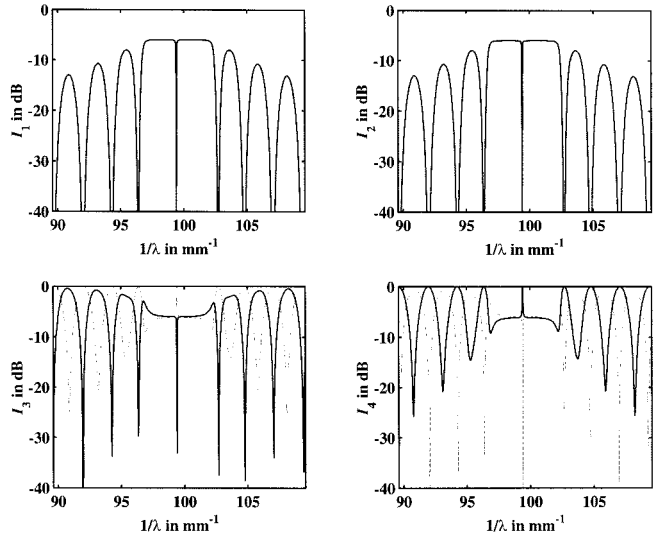

Fig. 2. Output intensity characteristics at the four ports of the M–Z interferometer, normalized with respect to the input intensity at port 1. The solid (dotted) curves correspond to $l_2 = 10$ mm ($l_2 = 10$ mm + 3.38 μm) at a free space wavelength of $\lambda = 1.5$ μm.

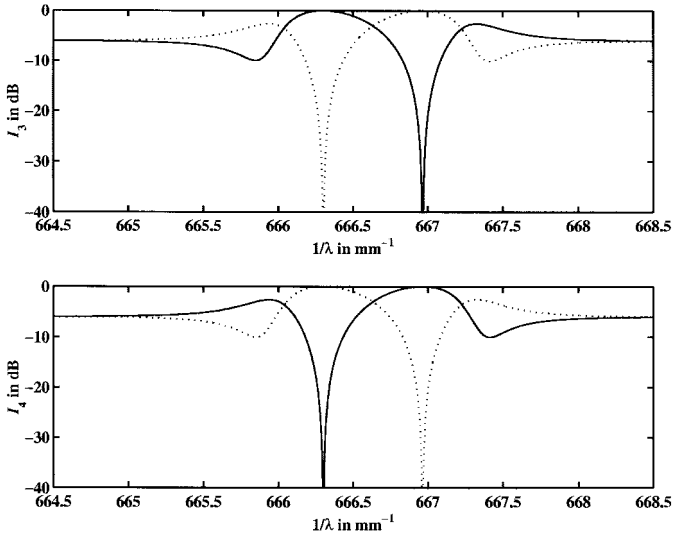

Fig. 3. Output intensities versus inverse wavelength of a M–Z interferometer incorporating a superstructure. The solid (dotted) line corresponds to $l_2 = 10$ mm ($l_2 = 10$ mm + 2.50 μm).

Fig. 2 shows the output intensities at the four ports of the device, normalized to the input intensity at port 1 as a function of free-space wavelength (I_1–I_4). The solid (dashed) curve corresponds to $l_2 = 10$ mm (10 mm + 3.38 μm). The slight change in l_2, corresponding to approximately 180° phase shift, causes the output at port 3 to drop by more than 40 dB and the output at port 4 to increase from an imperceptibly low level to full input level. Calculation shows that, as expected, as the phase shift in the l_2 arm varies from 0° to 360°, the drop in level at port 3 varies from zero to a maximum of over 40 dB at 180°, and back to zero. The effect of the F–P resonator is the marked reduction of the bandwidth over which this transition occurs. The width of the central spike in Fig. 2 is approximately 1 nm, corresponding to a bandwidth of 2 GHz. By adjusting the length of the F–P cavity, the location of the spike can be shifted. The out-of-band behavior of this sensor can also be seen in Fig. 2, where we notice that a phase shift of 180° inverts the outputs of ports 3 and 4. When the phase shift is a multiple of 2π, the two curves are identical. The reflected intensities observed at ports 1 and 2 are not affected by the phase change in the l_2 arm. From the reflection coefficient of the F–P resonator, computed at the center of its resonance, the coupling coefficient in the Bragg gratings is estimated to be 0.02 μm^{-1}. At center wavelength (10.04 μm), only the dotted output at port 3 (corresponding to 180° phase shift) is sensitive to variations in the coupling coefficient K. As the common coupling coefficient is varied from 0.4 to 0.5, the dotted output drops from -13 dB to below -40 dB and subsequently rises again to -13 dB as K is further increased to 0.6.

Characteristics indistinguishable from those shown in Fig. 2 are obtained in the stopband region, when distributed parameter rather than lumped-element couplers are used. Care must be taken to select their length appropriate for an equal power split. We have chosen a β/κ ratio of 30 and a length of

$$l = \frac{\pi}{4\kappa} = \frac{30\pi}{4\beta} = \frac{30\lambda_0}{8n_e} = 25.1\ \mu\text{m} \tag{1}$$

to obtain the same output intensities as those shown in Fig. 2.

We simulated a lossless device similar to that shown in Fig. 1, replacing the F–P resonator by a so-called superstructure consisting of a series of five gratings with 60, 138, 157, 138, and 60 unit cells. The period length was $\lambda = 0.5$ μm, the gap separating the gratings was also 0.5 μm, and the high and low refractive indexes were chosen to be $n_h = 1.51$ and $n_l = 1.49$, respectively. The bandwidth of this composite grating is approximately 1.45 nm, centered at 1.5 μm. Note that throughout this paper, we shall use normalized frequency (inverse wavelength) units $f_{\text{norm}} = f/c = 1/\lambda$, where c, the velocity of light in vacuum is given in millimeters per second so that the length dimensions in our computer program are interpreted to be in millimeters. In doing so, the product of the normalized frequency and nominal length provide the ratio of the physical length to the free-space wavelength. Fig. 3 shows the output intensities versus inverse wavelength at ports 3 and 4. The solid curve applies to the circuit when $l_2 = l_4 = 10$ mm, the dotted curve reflects a change in l_2 by 2.5 μm. The wavelength separation is 1.35 nm. Reflected intensities were both down by more than 36 dB.

The channel combining/dropping (add/drop) filter is another example of a cascaded interferometric circuit. In its simplest form, it consists of two forward (Type 1) couplers separated by identical Bragg gratings (band-stop filters) in the connecting waveguides. Assuming port 1 to be the input port, the distance between the output ports of the first coupler and gratings must be such as to cause a constructive (destructive) interference for the reflected signals traveling back toward port 2 (port 1). If the couplers are 3-dB hybrids, this condition is fulfilled when the phase-delay difference between the output ports of the first coupler and gratings is $N\pi$, where N is an integer. Similarly, the distances between the output ports of the gratings and the

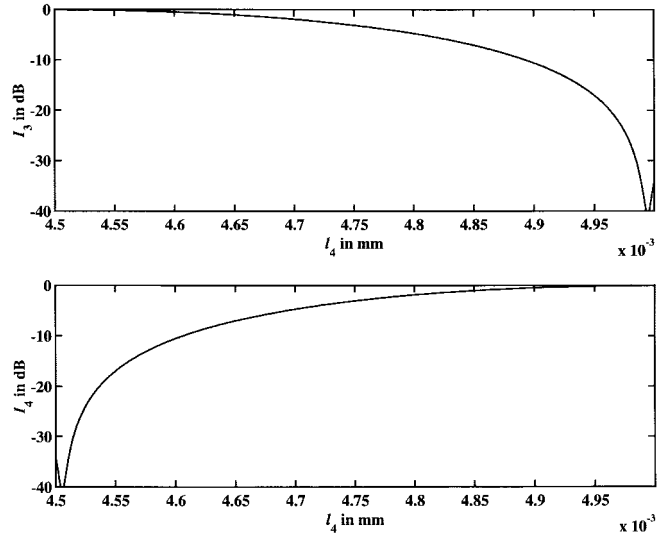

Fig. 4. Out-of-band outputs of a channel combining/dropping filter as a function of the waveguide length connecting the output of a grating with the input of a second coupler. The length of a grating period is 0.5 μm.

input ports of the second coupler can be selected to cause the transmitted signal to exit through either ports 3 or 4 of the device.

Fig. 4 illustrates the effect of path-length (l_4) variation between one of the gratings and the second coupler, while keeping the corresponding path length (l_3) behind the other grating fixed at 5 μm. Here, the applied frequency is in the passband of the gratings ($\lambda = 0.5$ μm, $n_e = 1.5$). As l_4 increases from 4.5 to 5 μm, the output is gradually transferred from ports 3 to 4; when l_4 is 4.75 μm, the power is split equally between the two output ports.

Another type of channel dropping/combining filter, developed for millimeter-wave use by Ohtomo (Ootomo) *et al.* [3] and for optical frequency division multiplexing (FDM) communication systems by Oda *et al.* [4], consists of two or more ring resonators coupled to each other and to external waveguides. A double-ring resonator version and its equivalent circuit are shown in Fig. 5(a) and (b), respectively. For an input signal at port 1, there is output at ports 2 and 4 only. Output at port 4 occurs only in the narrow bands of resonance of the coupled rings. For resonance to occur,

$$k_0 n_{e,i} L_i = \frac{2\pi f}{c} L_{\text{eff},i} = 2\pi N_i, \qquad i = 1, 2 \tag{2}$$

must be satisfied, where N_i is an integer. The free spectral range (FSR) of the ith ring is $\text{FSR}_i = c/L_{\text{eff},i}$. In the symmetric design $K_1 = K_3$, and the rings are identical. In the so-called vernier configuration, N_1/N_2 is the ratio of two consecutive integers ≥ 2. Since resonance requires that (2) be satisfied for all rings, the FSR of the combined device becomes the smallest common denominator of all FSR_i. For example, if $\text{FSR}_1 = 30$ and $\text{FSR}_2 = 40$, then the coupled resonator will have an FSR $= 120$. As the full width at half maximum (FWHM) is not affected by this operation, the vernier configuration offers a practical tool to increase the finesse of the filter.

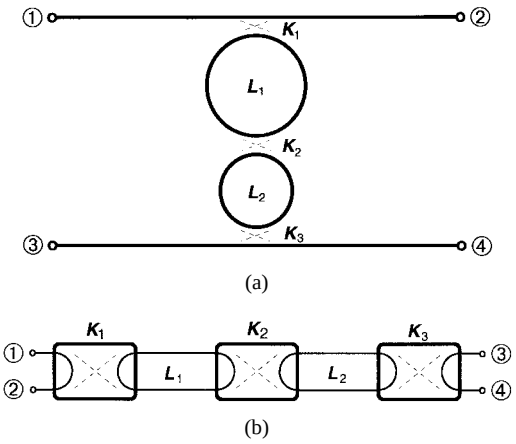

Fig. 5. Double-ring-resonator channel combining/dropping (a) filter. (b) Its equilvalent circuit. Modeled using concatenated Type-5 couplers.

The level of coupling between the resonant rings determines whether the resonators are undercoupled, critically coupled, or overcoupled. Oda *et al.* [4] determined the critical power-coupling coefficient for a symmetric device to be

$$K_{2,\text{crit}} = \left[\frac{K_1}{2 - K_1}\right]^2. \tag{3}$$

For $K_2 > K_{2,\text{crit}}$ the filter is overcoupled and its resonance curve acquires two peaks. For a symmetric double-ring filter, we found the split between the peaks to be well approximated by

$$\Delta f = \frac{c\sqrt{K_2 - K_{2,\text{crit}}}}{\pi L_{\text{eff}}}. \tag{4}$$

The device is very sensitive to coupler loss, but it tolerates waveguide loss up to 1 dB/cm without significant deterioration of the amplitude characteristics.

The performance of multiple-ring add/drop filters is often enhanced by mirror or grating-assisted feedback. These configurations will be discussed in greater detail in Section III.

III. Feedback-Assisted Interferometric Circuits

A simple feedback-assisted interferometer [5] and its equivalent are shown in Fig. 6. Use of a Type-3 coupler facilitates "straightening out" the convoluted configuration into what has been classified in Part I as a Case-4 feedback-assisted cascaded network. The device includes one resonant ring consisting of the l_2 and l_3 waveguides. The presence of a resonant ring results in a comb-like frequency characteristic with an FSR determined by the effective length of the ring $L_{\text{eff}} = \sum_i l_i n_i$. Resonance occurs when the round-trip phase is an integral multiple of 2π, i.e., when

$$k_0 L_{\text{eff}} \pm p\frac{\pi}{2} = \frac{2\pi f}{c} L_{\text{eff}} \pm p\frac{\pi}{2} = 2\pi N \tag{5}$$

where p is the number of coupled connections in the path, each inserting a 90° phase shift, and N is an integer.

The characteristics of the normalized transmitted (I_2) and reflected (I_1) intensities as a function of the normalized frequency are shown in Fig. 7. The circuit components are

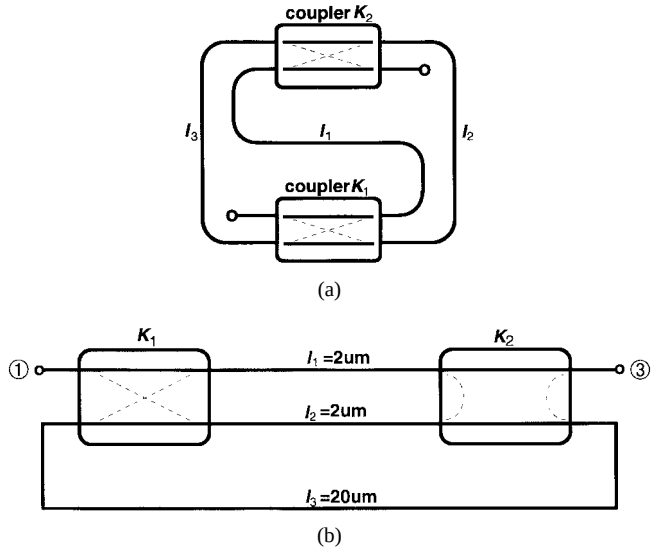

Fig. 6. A feedback-assisted two-coupler interferometer. (a) The fiber-optic device. (b) The equivalent circuit.

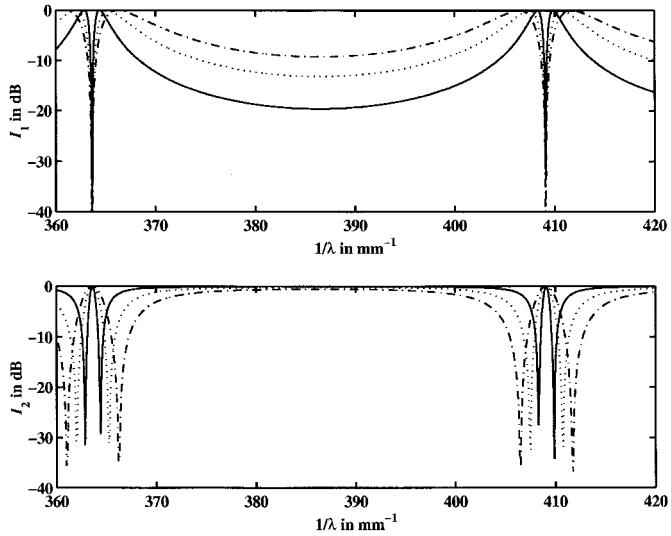

Fig. 7. Normalized reflected and transmitted intensities versus inverse wavelength (f/c) of the device shown in Fig. 6. The parameter is the common power-coupling coefficient K. Solid curve: $K = 0.1$, dotted curve: $K = 0.2$, and dashed-dotted curve: $K = 0.3$. The other parameters of the device are given in the text.

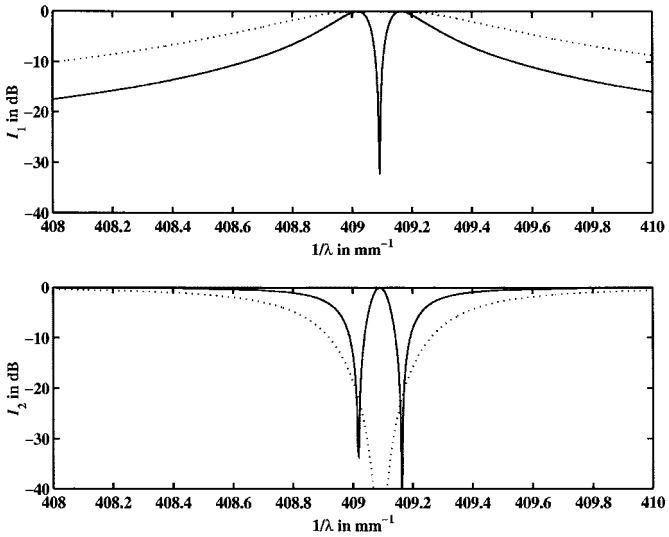

Fig. 8. Normalized reflected and transmitted intensities versus inverse wavelength (f/c) of the device shown in Fig. 6. For the solid (dotted) line $K_2 = 0.01$ (0.057). In both cases, $K_1 = 0.01$.

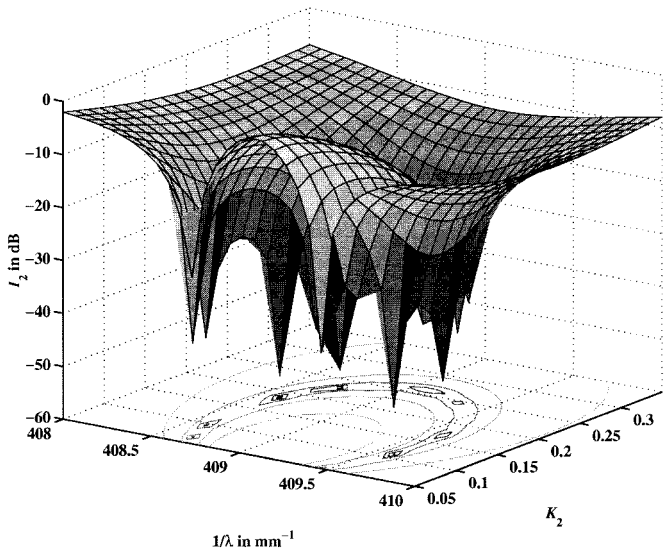

Fig. 9. Normalized output intensity of the device shown in Fig. 6, as a function of the inverse wavelength and K_2. The value of K_1 was kept constant at 0.05.

lossless, the refractive index of the guides is $n_e = 1$, $p = 0$, and $L = l_2 + l_3 = 22$ μm. For these values, the two resonances shown correspond to $L/\lambda = 8$ and 9, respectively, and the FSR evaluates to $\Delta f \sim 1.36 \times 10^{13}$ Hz, or 45.45 units on the inverse wavelength scale. The resonant wavelengths of this device are insensitive to variations in l_1. The parameter in Fig. 7 is the common power-coupling coefficient of the couplers $K_1 = K_2 = K$, which has been varied from 0.1 to 0.3 (10–5.3 dB). As K increases, so does the width of the passband δf. For $K = 0.1$, this passband is approximately 0.649 units ($\sim 1.95 \times 10^{11}$ Hz) wide at the -3-dB level. The finesse of the interferometer with $K = 0.1$ is

$$F = \frac{\Delta f}{\delta f} \cong 70. \tag{6}$$

With $K = 0.05$, the finesse obtained is 150.

Another feature of this circuit is illustrated in Fig. 8, where the frequency characteristics of the reflected and transmitted intensities are plotted for $K_2 = 0.01$ (solid line) and 0.057 (dotted line), while $K_1 = 0.01$. A narrow and extremely pronounced (>40 dB) discrimination occurs at the resonance frequency as a result of a small change in K_2. This feature can be exploited to sense the presence or absence of a mesurand that affects the coupling coefficient of a weak coupler. The surface plot of Fig. 9 illustrates the variation of the output as a function of inverse wavelength and K_2. Notice the sharp dips in the output intensity distributed over an elliptical path on the K_2 versus normalized frequency plane. In this simulation, K_1 was set to 0.05 (13 dB) and losses were neglected.

The circulating wave intensity in the feedback line can be computed using the expressions given in [1, Appendix C].

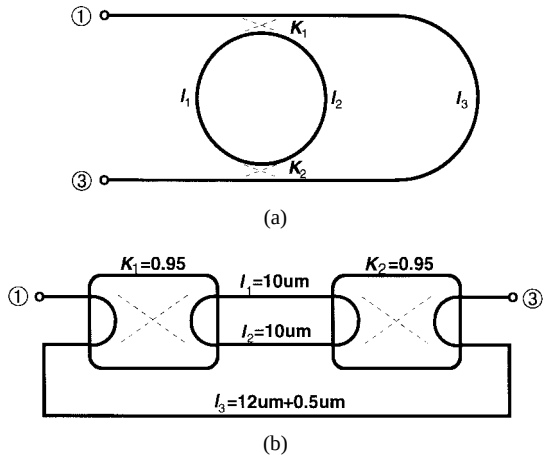

Fig. 10. (a) Feedback-assisted ring resonator. (b) Its equivalent network.

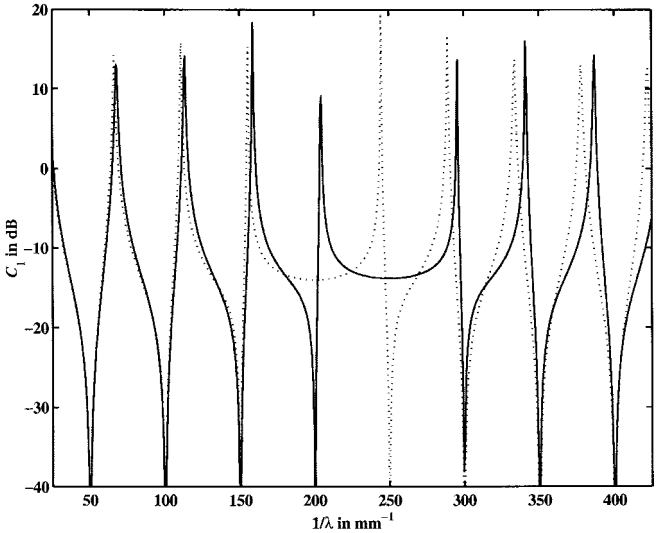

Fig. 11. Characteristics of the forward wave intensity in the feedback guide of the ring resonator illustrated in Fig. 10. Resonances occur when the phase delays in paths l_2 and l_3 are commensurate. The common coupling coefficient is $K + 0.95$ and the length of the feedback guide is 12 μm (solid line) or 12.5 μm (dotted line). Other parameters are listed in the text.

Calculations show that, at resonance, this circulating wave intensity can rise more than 30 dB over the level maintained between resonances.

A feedback-assisted ring resonator and its equivalent network, incorporating two Type-5 couplers in a Case-4 configuration, are shown in Fig. 10. Here, we note that when the generalized coupler described in Part I is applied to model a device, the equivalent circuit may not be unique. This multiplicity of equivalent circuits for the same device is in the nature of modeling. Since true equivalents produce identical numerical results, it is immaterial which model is adopted. For example, replacing both couplers with Type 1 in Fig. 10(b), and appropriately renaming the connecting waveguides, or replacing the second coupler with Type 4 and changing the feedback configuration to Case 5, result in other equivalent circuits of the device depicted in Fig. 10(a).

The ring resonator shown in Fig. 10 is a unit-transmittance interferometer, which means that under ideal conditions, i.e., when the components are lossless and the splices are perfect, all input power will exit at the output port. Consequently, the output frequency characteristics of an ideal unit-transmittance device is flat. However, large wave-intensity variations are observed in the feedback line (l_3) when the input frequency is commensurate with the resonant frequency of the ring [6]. This can be seen in Fig. 11, illustrating the forward wave intensity (C_1) in the feedback guide (there is no power flow in the reverse direction) as a function of inverse wavelength. In this simulation, the ring consisted of two $K = 0.95$ coupling coefficient couplers, equal half-rings $l_1 + l_2 = 20$ μm, and a feedback guide $l_3 = 12$ μm-long (12.5 μm) represented by the solid (dotted) line. With $n_e = 1$, the first resonance at $N = 1$, calculated from (2), occurs at $1/\lambda = 50$. Notice that there is no coupling into the ring for a normalized frequency of 250 (200) or $N = 5$ ($N = 4$). This is due to the incommensurate traveling times in the half-ring and feedback line. Whenever

$$N_{\text{feedback}} l_{\text{ring}} n_{\text{ring}} = 2N l_{\text{feedback}} n_{\text{feedback}} \tag{7}$$

and N is of different parity from N_{feedback}, interaction between ring and feedback guide is eliminated as a result of a 180° propagation phase cancellation. In Fig. 11, the above equality holds true for $N = 5$ and $N_{\text{feedback}} = 6$ ($N = 4$ and $N_{\text{feedback}} = 5$), for $N = 15$ and $N_{\text{feedback}} = 18$ ($N = 12$ and $N_{\text{feedback}} = 15$), etc., but it does not hold, for example, for $N = 10$ and $N_{\text{feedback}} = 12$.

As expected, the Q factors associated with the resonances seen in Fig. 11 increase as $|K - 0.5|$ approaches 0.5, and are significantly reduced by coupler loss; however, they are remarkably insensitive to waveguide loss. A coupler attached to the feedback guide can sample resonant intensity fluctuations. Further examples of unit transmittance interferometric circuits are shown, e.g., in [7, Figs. 2 and 3].

We simulated several other feedback-assisted cascaded interferometers consisting of two 2×2 couplers. Those configurations that include one or more ring resonators exhibit comb-filter-type characteristics. The circulating wave intensity in the feedback line and the transfer characteristics of these interferometers are fairly complex, not only because (5) has as many sets of solutions as the number of resonant rings in the circuit, but also because the resonance frequencies of the rings shift as a result of coupling.

Here, we report on a circuit that exhibits useful circulating wave-intensity characteristics. A bulk-optic realization of the interferometer, comprised of four mirrors and two beam-splitters is shown in Fig. 12(a) [8], while the equivalent circuit appears in Fig. 12(b). This interferometer has one resonant ring that passes through l_1, l_2, and the two couplers, acquiring π phase shift in the process. All circuit components are assumed to be lossless. Fig. 13 illustrates a simulation of the output intensity as a function of the inverse wavelength and the common power-coupling coefficient $K_1 = K_2 = K$. For this figure, we have chosen $l_1 = 5$ μm, $l_2 = 15$ μm, $l_3 = 15$ μm and $n_e = 1.5$. The FSR is, therefore, $\Delta(1/\lambda) = 33.333$ units. A resonance occurs at $1/\lambda = 650$, which satisfies (5) with $N = 19$. Fig. 13 indicates a resonance bandwidth that gradually decreases in width as K approaches unity. The circulating wave intensity, normalized to the input intensity,

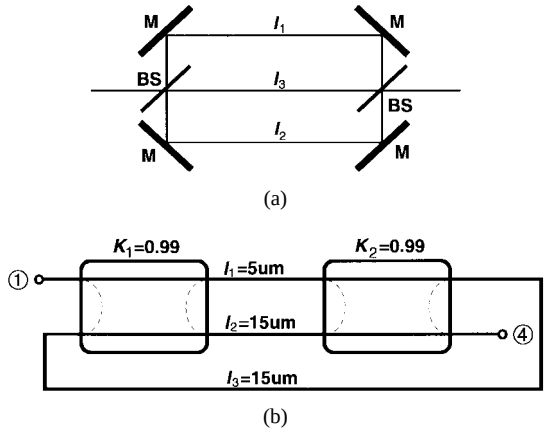

Fig. 12. (a) Resonant ring interferometer of another configuration. (b) Its equivalent circuit. BS: beam splitter, M: mirror. The resonant ring consists of paths l_1, l_2 and the two coupled connections in the couplers, each contributing 90° phase shift to the total phase delay.

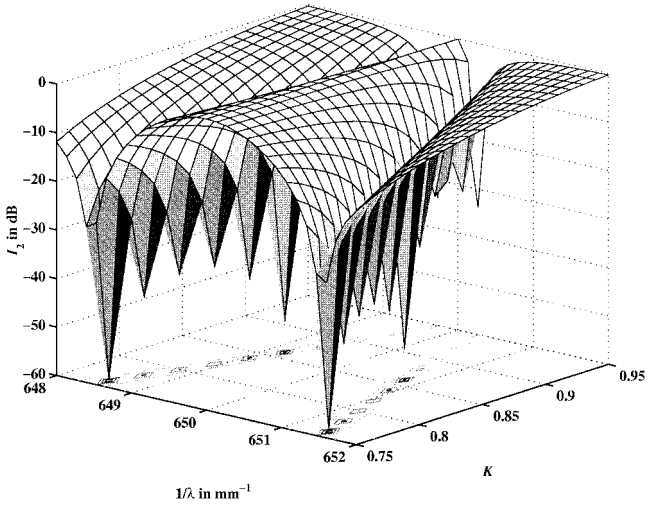

Fig. 13. Output intensity of the ring interferometer of Fig. 12 as a function of inverse wavelength and the common power-coupling coefficient.

propagating in the feedback line l_3 is shown in Fig. 14. C_1 is the wave intensity propagating from ports 3 to 2 and C_2 is the wave intensity propagating in the opposite direction. The parameter is the common refractive index of the waveguides. For the solid curve, $n_e = 1.5$, for the dotted curve, $n_e = 1.500\,75$, and for the dashed–dotted curve, $n_e = 1.5015$. The common power-coupling coefficient is $K = 0.99$. The shift in the resonance frequency is in accordance with (5), i.e.,

$$\frac{\Delta f}{f} = -\frac{\Delta l_{\text{eff}}}{l_{\text{eff}}}. \tag{8}$$

Notice the narrow deep minima in the otherwise flat C_2 characteristics, centered on the resonance frequency. The result indicates that in this configuration 0.1% change in the refractive index causes an approximately 1.54-nm-wavelength shift at $\lambda_0 = 1.54$ μm. A directional coupler connected to the feedback line, sampling the current in the appropriate direction, should prove to be a sensitive tool to measure small variations in l_{eff}.

Application of the generalized scattering parameter algorithm described in Part I quickly reveals that circuits of seem-

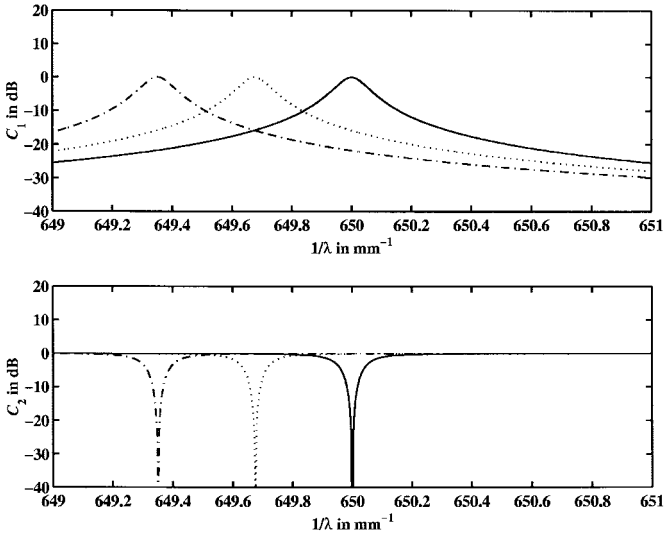

Fig. 14. Spectral characteristics of the circulating wave intensities in the feedback path l_3 of Fig. 12 propagating from ports 3 to 2 (C_1) and from ports 2 to 3 (C_2). The parameter is the common effective refractive index of the waveguides. Solid line: $n_e = 1.5$, dotted line: $n_e = 1.500\,75$, and dashed–dotted line: $n_e = 1.5015$. The common power-coupling coefficient is 0.99.

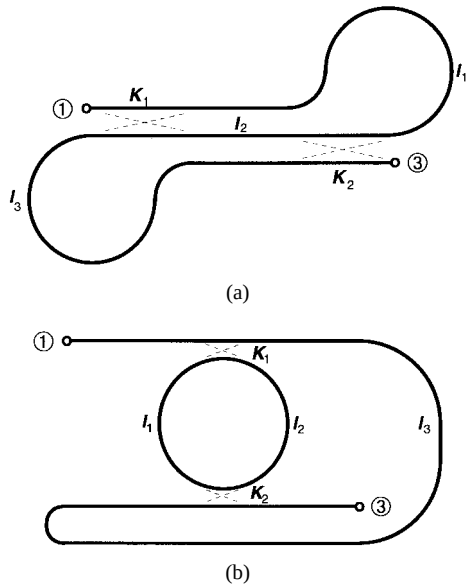

Fig. 15. Two resonant ring interferometers that exhibit similar input/output characteristics as the circuit shown in Fig. 12. Only Fig. 15(b) displays the sharply resonant circulating current characteristics of Fig. 14. Neither circuit is of unit transmittance.

ingly quite different topology can have identical input/output characteristics. For example, the double-ring interferometer shown in Fig. 15(a) with $K_1 = K_2 = 0.99$, and the ring resonator shown in Fig. 15(b) [9], a modified version of the ring resonator seen in Fig. 10 with $K_1 = K_2 = 0.01$, have the same input/output characteristics as the circuit shown in Fig. 12. However, only Fig. 15(b) exhibits the narrow-band circulating current characteristics seen in Fig. 14.

We simulated switching discrimination in excess of 40 dB at discrete equally spaced frequencies on a lossless interferometer of two cascaded couplers in a Case-6 configuration. The first

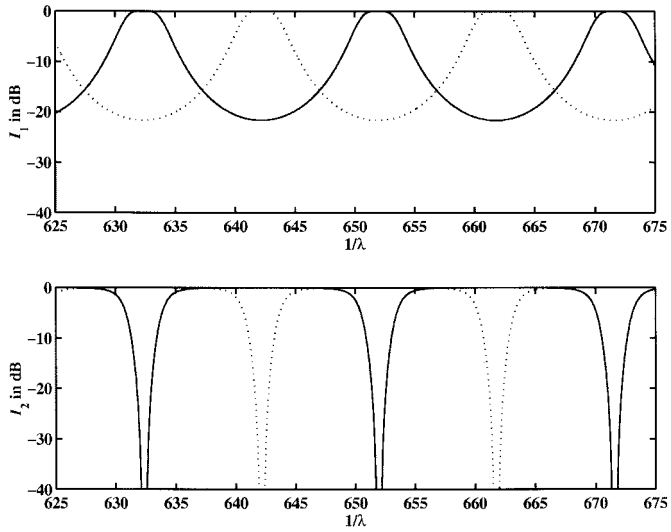

Fig. 16. Reflected and transmitted intensity characteristics of a cascaded network in Case-6 configuration described in the text. Notice the more than 40-dB switching discrimination at discrete frequencies when the power-coupling coefficient of the second coupler is changed from 0.04 (solid curve) to 0.96 (dotted curve). The coupling coefficient of the first coupler is $K_1 = 0.44$.

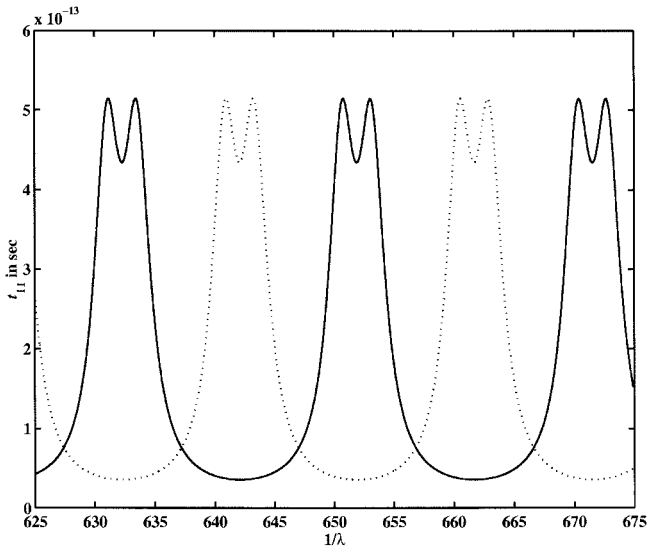

Fig. 17. Group-delay characteristic of the reflected signal of the interferometric network to which Fig. 16 applies. $K_2 = 0.04$ (solid line), $K_2 = 0.96$ (dotted line), and $K_1 = 0.44$.

coupler was Type 3, the second Type 1. The reflected and transmitted intensities are shown in Fig. 16. For the solid curve, $K_2 = 0.04$, for the dotted curve, $K_2 = 0.96$, and $K_1 = 0.44$ in both cases. No appreciable deterioration of this performance was observed until waveguide losses reached 10 dB/cm or coupler losses reached $a = \sqrt{1-\gamma} = 0.98$ ($\gamma = 0.04$). Note that for integrated circuits in Si, the actual waveguide loss is approximately 0.1 dB/cm, while in fiber waveguides a much smaller loss coefficient can be realized.

The group delay for this circuit, computed using (27) of Part I, appears in Fig. 17. Here, we note that for a lossless reciprocal two-port, the phase angles of S_{11}, S_{12}, and S_{22} are related through

$$\phi_{12} = \frac{1}{2}(\phi_{11} + \phi_{22}) + \frac{\pi}{2} \pm n\pi. \tag{9}$$

If the circuit is bilaterally symmetric, $\phi_{11} = \phi_{22}$ and, as a result, all three group-delay characteristics are the same. For asymmetric circuits, we observed a difference between ϕ_{11} and ϕ_{22}, but it was so small, that the relative difference it caused between τ_{11} and τ_{22} was in the order of 10^{-4} and could not be registered.

An interferometer consisting of a cascade of a Type-4 (or Type-5) and Type-1 coupler in Case-6 configuration can be used to obtain extremely narrow-band rejection at the output port. This circuit includes two resonant rings, both passing through the guides connecting the couplers (l_1 and l_2) and the feedback line (L), but one of the paths acquires an extra 180° phase shift by passing through the second coupler twice. As a result, the output frequency characteristics consists of two interspersed comb distributions whose separation depends on the coupling coefficient of the Type-1 coupler. In our simulation, both couplers had a power-coupling coefficient of 0.05 (13 dB). We found the 3-dB relative bandwidth to be 2.3×10^{-4}, which reduces to 4.6×10^{-5} when the coupling coefficient drops to 0.01 (20 dB). The length of the feedback

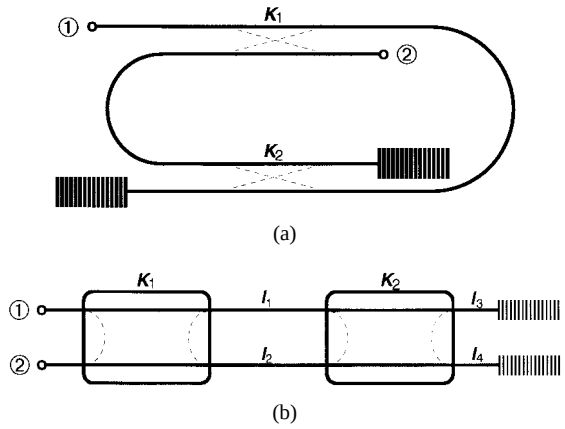

Fig. 18. (a) Switching comb-filter configuration. (b) Its network equilvalent, consisting of two cascaded couplers and Bragg grating terminations at ports 3 and 4.

guide can control the center wavelength of the spike. We investigated the effect of losses on this filter and found that waveguide loss up to 0.1 dB/cm had insignificant influence on its performance; however the device was extremely sensitive to coupler loss. Specifically, we observed that $a = 0.999$, or $\gamma = 2 \times 10^{-3}$ was the maximum value tolerable for a useful device (20-dB rejection).

A switching comb filter operating over the stopband of a grating has been simulated using the configuration shown in Fig. 18. The circuit is made from two lengths of coupled optical fibers, each equipped with a Bragg grating at one end [see Fig. 18(a)]. The equivalent circuit consists of two cascaded Type-3 couplers in Case-3 configuration [see Fig. 18(b)]. Two resonant rings characterize the performance of this network. For the first, $l_{\text{eff}} = (l_1 + l_2)n_e$ and it passes through two coupled links, while the second passes through one coupled link with $l_{\text{eff}} = 2(l_1 + l_2 + l_3 + l_4 + 2d)n_e$, where d is the penetration depth of the signal into the grating at the frequency where the resonance occurs. The distance d is associated with

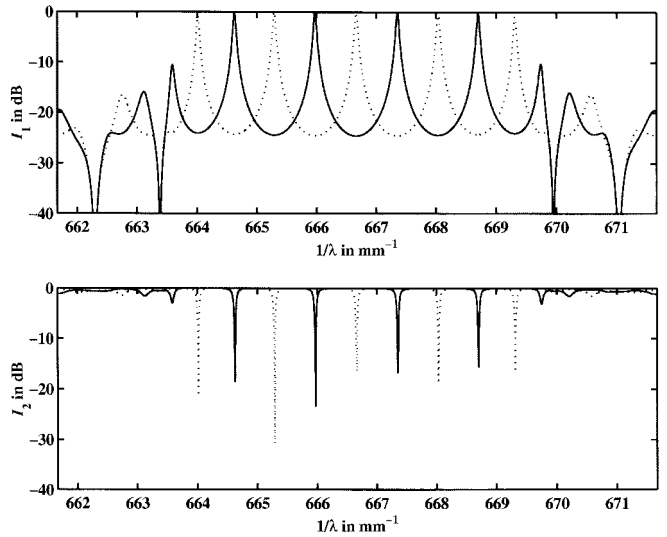

Fig. 19. Reflected and transmitted intensity characteristics of the comb-filter device shown in Fig. 18. The common coupling coefficient is 0.5. A $\pi/2$ phase shift in l_3 or l_4 moves the solid curve into the dotted one. Other pertinent parameters are given in the text. Higher resolution sampling reveals that the transmission minima reach below -40 dB.

the reflection time delay τ, thus,

$$d = \frac{1}{2}\tau v_p = -\frac{1}{2} v_p \frac{\partial \phi}{\partial \omega} \tag{10}$$

where ϕ is the phase of the reflection coefficient (S_{11}) and v_p is the phase velocity in the grating.

The gratings were selected to be identical: periodicity $\Lambda = 0.5$ μm, high/low refractive indexes of 1.51/1.49 and $N_G = 200$ unit cells. Fig. 19 shows the reflected (I_1) and transmitted (I_2) intensity characteristics for $K_1 = K_2 = 0.5$, $l_1 = l_2 = 10$ μm, and $l_3 = l_4 = 100$ μm (solid line). Using the parameters given above, we obtain a frequency separation of 33.33 units for the first set of resonances, and approximately 1.3 units for the second set (the calculated penetration depth at stopband center is $d = 18.5$ μm). None of the first set of resonances falls within the stopband of the gratings, which is centered on $N = 20$. Fig. 19 indicates that the second set of resonances determine the characteristics of the filter. A $\pi/2$ phase shift in l_3 or l_4 moves the solid-line characteristics into the dotted one, effectively providing more than 20-dB discrimination. At the given wavelength ($\lambda_0 = 1.5$ μm) and effective refractive index ($n_e = 1.5$), such a phase shift is produced by $\Delta n_e = 3.75 \times 10^{-3}$, or a displacement of 0.25 μm.

Spectral characteristics very similar to those seen in Fig. 19 have also been obtained using distributed rather than lumped-element couplers having 13.98-μm length and a β/κ ratio of 1.252.

As a final application of the generalized analysis to feedback-assisted cascaded coupler circuits, an add/drop filter, shown in Fig. 20(a), is described. The equivalent circuit is seen in Fig. 20(b). The gratings sharpen the resonance provided by the ring and offer two orders of magnitude higher selectivity than that which can be obtained by simply terminating ports 3 and 4 with wavelength independent reflectors (mirrors). For our simulation, an effective guide index of 1.5 was used, the

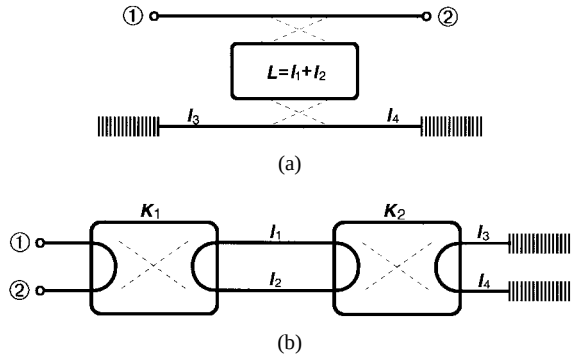

Fig. 20. (a) A Bragg-grating assisted ring resonator add/drop filter. (b) Its network equivalent, consisting of Type-5 couplers.

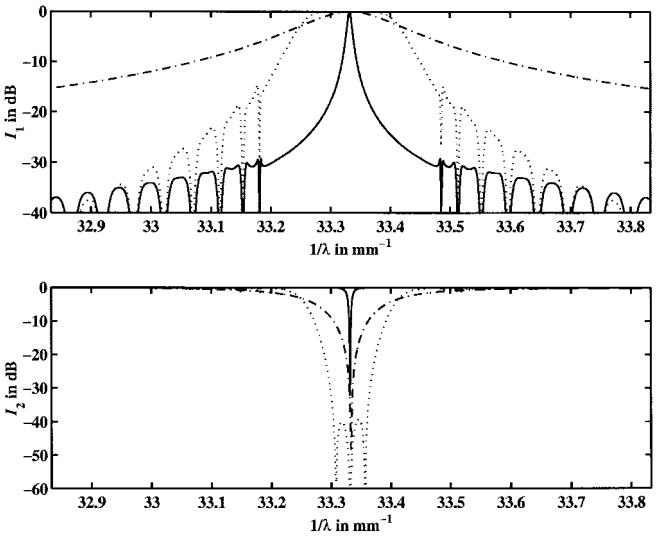

Fig. 21. Reflected and transmitted intensity characteristics of the add/drop filter shown in Fig. 20. Solid line: $K_1 = 0.5$, dotted line: $K_1 = 0.032$, dashed–dotted line: $K_1 = 0.032$, and mirrors replace the gratings. In all three cases, $K_2 = 0.01$. Additional parameters are specified in the text.

length of the ring was $L = 20$ μm, the waveguides connecting the gratings to the second coupler were $l_3 = l_4 = 5$ μm long, and the gratings had $N_G = 300$ unit cells with $\lambda = 10$ μm periodicity and high/low refractive indexes of 1.51/1.49. The free-space wavelength at resonance for this device is $\lambda_0 = 30$ μm. Fig. 21 shows three reflection (I_1) and transmission (I_2) intensity characteristics. The solid line is obtained when $K_1 = 0.5$, the dotted line corresponds to $K_1 = 0.032$, and the dashed–dot line applies to a filter with mirrors replacing the gratings and $K_1 = 0.032$. In all three cases, $K_2 = 0.01$. Both couplers and waveguides were assumed loss free.

Fig. 21 indicates the versatility of this filter configuration when the grating stopband is tuned to the resonance of the ring. A further fivefold reduction of the 3-dB bandwidth of the I_2 characteristics can be obtained by lengthening (or shortening) L by 10%, causing less than 5×10^{-5} relative shift in the resonance frequency. It is also possible to move the resonant dip over the stopband of the grating by varying the length of l_3 or l_4. This is illustrated in Fig. 22, where l_4 is changed from 3 μm (dotted line) to 5 μm (solid line) to 7 μm (dashed–dotted line). The device is relatively insensitive to waveguide loss,

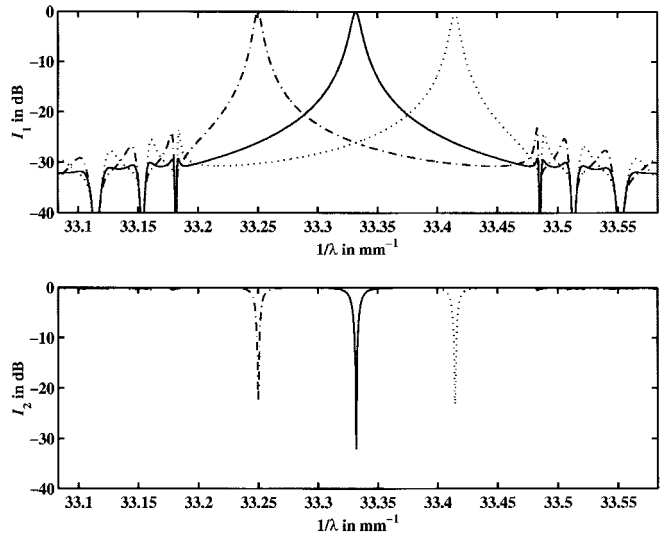

Fig. 22. Characteristics of the add/drop filter of Fig. 20 with changing guide length l_4. Dotted line: $l_4 = 3$ μm, solid line: $l_4 = 5$ μm, and dashed-dotted line: $l_4 = 7$ μm. Higher resolution sampling reveals that the transmission minima reach below -40 dB.

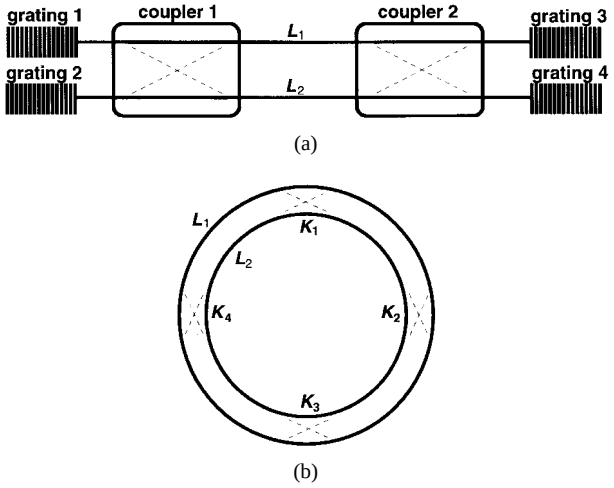

Fig. 23. The two types of symmetrical resonator circuits investigated. (a) Option-1 configuration with all four ports terminated by identical gratings. (b) Option-5 configuration where the feedback lines connect the output of the cascaded network with its input, creating an endless loop.

but very sensitive to coupler loss. As an add/drop filter, this ring resonator would be used in conjunction with a circulator.

IV. Resonator Circuits

Interferometric resonator circuits constructed from a chain of 2×2 couplers have all four ports of the cascaded network either terminated by mirrors or gratings and/or connected by feedback circuits. Resonance occurs when

$$\det[\boldsymbol{I} - \boldsymbol{S}\boldsymbol{S}_E] = 0 \tag{11}$$

where $\boldsymbol{S}$ is the scattering matrix of the cascaded network, $\boldsymbol{S}_E$ is the scattering matrix of the embedding network defined in Part I, and $\boldsymbol{I}$ is the 4×4 identity matrix. Unless the resonator is lossless, (11) cannot be satisfied. Instead, we seek a minimum of the absolute value of the left-hand side.

Seven resonator configurations, called "Options," were defined in Part I. In Option 1, all four ports are individually terminated by reflective elements, numbered from 1 to 4. In Options 2–4, there are two reflectors named after the port they terminate and one feedback line L. In Options 5–7, there are two feedback lines connecting the four ports. The line attached to port 1 is designated as L_1, the other is designated as L_2.

Interferometric resonator networks usually are comprised of more than one resonant ring. Were they uncoupled, each ring would resonate at a series of resonant frequencies determined by (5). Coupling between two identical resonators or between resonators whose resonant frequencies are close to each other causes their resonant frequencies to push apart [10], as discussed in connection with (4). The stronger the coupling, the greater the separation between the resonant frequencies. This general rule undergoes some modification in resonator circuits where several sets of resonances are likely to interfere with each other.

To simplify the problem, we investigated two types of resonators consisting of identical couplers: cascaded couplers terminated at all four ports by identical gratings (Option 1) and symmetric resonant rings (Option 5). Fig. 23 shows examples of these circuits. Fig. 23(a) illustrates a resonator in Option-1 configuration consisting of two identical Type-1 couplers; L_1 and L_2 represent the entire distance between the gratings facing each other. Fig. 23(b) shows four cascaded Type-1 couplers in Option-5 configuration where the feedback lines connect the output of the cascaded circuit with its input, creating an endless loop. L_1 and L_2 represent the entire length of the rings. The number of cascaded couplers N_C and the type of coupler used are arbitrary in either configuration.

To demonstrate the salient features of the type of resonators shown in Fig. 23(a), we have chosen a network consisting of two Type-1 couplers connected by waveguides with an effective refractive index of 1.5, total lengths of $L_1 = 150$ μm and $L_2 = (150 + \delta)$ μm, and terminated by gratings defined by $\Lambda = 0.5$ μm, $n_h/n_l = 1.51/1.49$, and $N_G = 200$. The couplers were positioned so that the lengths L_1 and L_2 were divided into equal sections and the length increment of the second guide δ was varied from 0 to 1.5 μm. Visual inspection reveals that this circuit incorporates four resonant loops with the following round-trip lengths: $2L_1 + 2\delta + 4d$, $2L_1 + 4d$, $2L_1 + 2\delta/3 + 4d$, and $2L_1 + 4\delta/3 + 4d$. When the coupling is negligible, only two resonances corresponding to the first two round trips occur. With $L_1 = 150$ μm and $\delta = 0$, these will overlap and provide a set of resonances in the grating stopband separated by FSR $= 1.7825$ units on the inverse λ scale. Since 180° phase shift in this circuit is obtained for a change of 0.5 μm in round-trip length, setting $\delta = 0.25$ μm will result in a second set of resonances bisecting the first. With increased coupling, the third and fourth set of resonances will also appear, their location being determined by δ and by the strength of the coupling. Fig. 24 was obtained for $K_1 = K_2 = 0.5$ and $\delta = 0$ (solid line), $\delta = 0.75$ μm (dotted line), and $\delta = 1.5$ μm (dashed–dotted line). Note that the dips reaching down to only about -4 dB is merely an indication that the number of sampling points used in the computer program were insufficient to adequately resolve the sharp resonances.

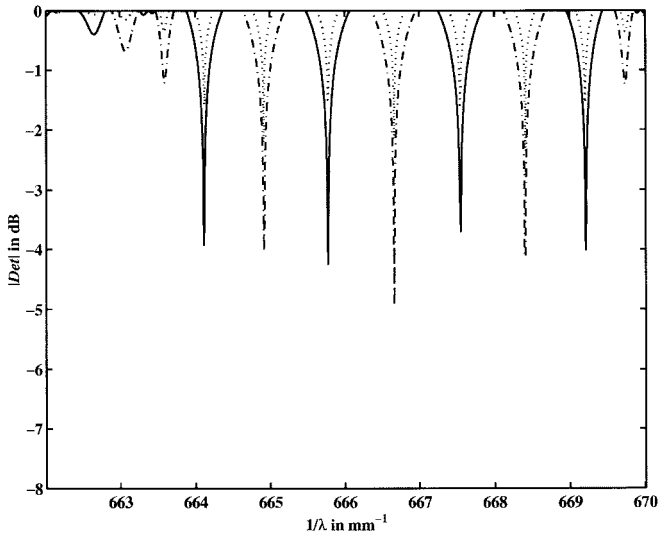

Fig. 24. Set of resonances occurring in the stopband of the gratings for the device shown in Fig. 23(a). $L_1 = 150$ μm, $L_2 = (150 + \delta)$ μm, $K_1 = K_2 = 0.5$. Solid line: $\delta = 0$, dotted line: $\delta = 0.75$ μm, and dashed–dotted line: $\delta = 1.5$ μm. Higher sampling rates are required to better resolve the sharp resonances.

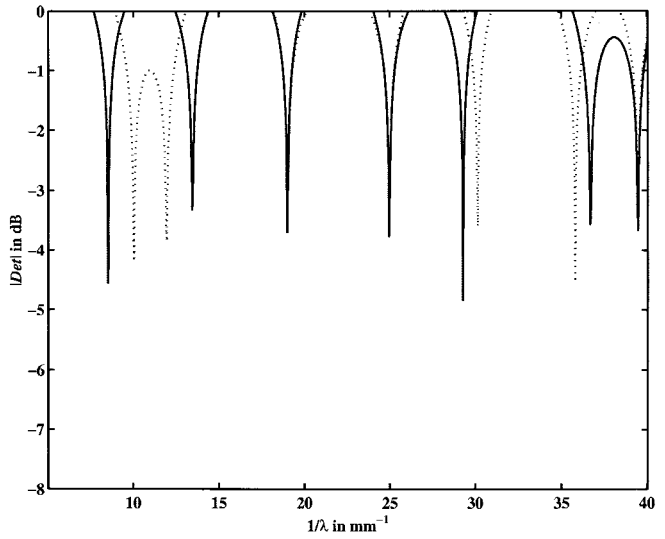

Fig. 25. Resonance characteristics of the device shown in Fig. 23(b) with four couplers. The common power-coupling coefficient is 0.1, $L_1 = 100$ μm, $L_2 = 83.333$ μm. Solid line: forward (Type 1) couplers, dotted line: reverse (Type 3) couplers.

For the configuration shown in Fig. 23(b), we have chosen $n_e = 1$ and ring lengths of $L_1 = 100$ μm and $L_2 = 83.333$ μm. With these parameters, the uncoupled resonances occur at multiples of ten and 12 inverse wavelength units, respectively. When $N_C = 2$, changing forward couplers (Type 1) into reverse couplers (Type 3) causes no change in the performance because the circulating paths remain the same. This is no longer the case when $N_C > 2$. For the results shown in Fig. 25, $N_C = 4$ and a common power-coupling coefficient of 10 dB was chosen. The solid line applies to Type-1 couplers, the dotted line to Type-3 couplers. There is a coincidence of resonance frequencies at even multiples of the coupling-shifted fundamental resonances while odd multiples of the reverse coupler resonances remain practically unaffected by coupling.

We have chosen simple configurations to illustrate the salient features of resonant interferometric circuits. Of the type of losses that affect the resonant behavior, coupler loss is the most critical. We found that setting $a = 0.998$ ($\gamma = 0.004$) will significantly flatten the resonance dip. An equivalent effect is observed only when waveguide losses reach a level of 3.5 dB/cm.

V. Conclusions

In this paper we demonstrated, that the generalized analysis of interferometric networks based on 2×2 couplers is a powerful tool in the investigation of their performance characteristics. We also demonstrated the wide coverage of network topologies to which this analysis can be applied. All of the results were obtained using a single relatively simple (few 100 lines) MATLAB program that takes less than 1 min to run on a modern PC.

Simulations on a set of more complex configurations, fabricated with 2×2 couplers, have also been concluded and shall be reported in a forthcoming publication. One of these configurations are grating-assisted lattice networks, both uniformly and nonuniformly distributed, such as cascaded feedback-assisted interferometers, cascaded four-port couplers, and cascaded M–Z interferometers. The other type of network configuration treated can be characterized as a spectral filter; such as an M–Z interferometer with a feedback-assisted four-port in one its arms or a cascaded network where one of the four-port subassemblies is rotated by 90°.

References

[1] O. Schwelb, "Generalized analysis for a class of linear interferometric networks—Part I: Analysis," this issue, pp. 1399–1408.
[2] H. van de Stadt, "Ring interferometers with unit transmittance," *Appl. Opt.*, vol. 24, pp. 2290–2292, 1985.
[3] I. Ootomo, S. Shimada, and N. Suzuki, "Two-cavity ring-type channel-dropping filters for a millimeter-wave guided wave communication system," *IEEE Trans. Microwave Theory Tech.*, vol. MTT-19, pp. 481–484, May 1971.
[4] K. Oda, N. Takato, and H. Toba, "A wide-FSR waveguide double-ring resonator for optical FDM transmission systems," *J. Lightwave Technol.*, vol. 9, pp. 728–736, June 1991.
[5] Y. H. Ja, "Simultaneous resonance of an S-shaped two-coupler optical fiber ring resonator," *Opt. Commun.*, vol. 102, pp. 133–140, 1993.
[6] S. C. Hagness *et al.*, "FTDT microcavity simulations: Design and experimental realization of waveguide-coupled single-mode ring and whispering-gallery-mode disk resonators," *J. Lightwave Technol.*, vol. 15, pp. 2154–2165, Nov. 1997.
[7] S. Tedjini, A. Ho-Quoc, and D. A. M. Khalil, "All-optical networks as microwave and millimeter-wave circuits," *IEEE Trans. Microwave Theory Tech.*, vol. 43, pp. 2428–2434, Sept. 1995.
[8] Y. H. Ja, "A symmetric S-shaped double-coupler optical-fiber loop," *J. Modern Opt.*, vol. 37, pp. 1297–1317, 1990.
[9] Y. H. Ja, "A spectacles-shaped optical fiber ring resonator with two couplers," *Opt. Quantum Electron.*, vol. 23, pp. 379–389, 1991.
[10] E. Brenner and M. Javid, *Analysis of Electric Circuits*, 2nd ed. New York: McGraw-Hill, 1967, sec. 15.11.

Otto Schwelb (A'59–M'62–SM'85–LS'96), for photograph and biography, see this issue, p. 1408.